Full-Stokes polarization laser-induced breakdown spectroscopy detection of infiltrative glioma boundary tissue

GEER TENG,[1,2] QIANQIAN WANG,[1,3,4,6] QUN HAO,[1,4] AXIN FAN,[1] HAIFENG YANG,[5,7] XIANGJUN XU,[1,3,4] GUOYAN CHEN,[1,3] KAI WEI,[1,3] ZHIFANG ZHAO,[1,3] M. NOUMAN KHAN,[1,3] BUSHRA SANA IDREES,[1,3] MENGYU BAO,[1,3] TIANZHONG LUO,[1,3,4] YONGYUE ZHENG,[1,3] AND BINGHENG LU[1,3]

[1] *School of Optics and Photonics, Beijing Institute of Technology, Beijing, 100081, China*
[2] *Institute of Biomedical Engineering, Department of Engineering Science, University of Oxford, Oxford, OX3 7LD, United Kingdom*
[3] *Key Laboratory of Photonic Information Technology, Ministry of Industry and Information Technology, Beijing Institute of Technology, Beijing, 100081, China*
[4] *Yangtze Delta Region Academy of Beijing Institute of Technology, Jiaxing, 314033, China*
[5] *Department of Neuro-Oncology, Chongqing University Cancer Hospital, Chongqing, 400030, China*
[6] *qqwang@bit.edu.cn*
[7] *yanghaifeng@cqu.edu.cn*

Abstract: The glioma boundary is difficult to identify during surgery due to the infiltrative characteristics of tumor cells. In order to ensure a full resection rate and increase the postoperative survival of patients, it is often necessary to make an expansion range resection, which may have harmful effects on the quality of the patient's survival. A full-Stokes laser-induced breakdown spectroscopy (FSLIBS) theory with a corresponding system is proposed to combine the elemental composition information and polarization information for glioma boundary detection. To verify the elemental content of brain tissues and provide an analytical basis, inductively coupled plasma mass spectrometry (ICP-MS) and LIBS are also applied to analyze the healthy, boundary, and glioma tissues. Totally, 42 fresh tissue samples are analyzed, and the Ca, Na, K elemental lines and CN, C_2 molecular fragmental bands are proved to take an important role in the different tissue identification. The FSLIBS provides complete polarization information and elemental information than conventional LIBS elemental analysis. The Stokes parameter spectra can significantly reduce the under-fitting phenomenon of artificial intelligence identification models. Meanwhile, the FSLIBS spectral features within glioma samples are relatively more stable than boundary and healthy tissues. Other tissues may be affected obviously by individual differences in lesion positions and patients. In the future, the FSLIBS may be used for the precise identification of glioma boundaries based on polarization and elemental characterizing ability.

1. Introduction

Tumors or cancers, as the frightening names, have become one of the most serious causes of death in U. S. and even all over the world [1,2]. Although the incidence and mortality of cancer show a certain fluctuation between different genders and different races, the overall cancer population shows an upward trend [3]. Facing the tumors in the future, we still have many riddles need to figure out, for example, the time of deleterious mutation pathogenic, the tumor clone should be targeted, the right time for immunotherapy and so on [4]. However, no matter from what aspect we face and confront the tumor, precise diagnosis is one of the key problems during the therapy

process. Among these cancers and tumors, the brain tumor is a special one that need to pay attention on the precise diagnosis due to the lesion position.

Even though the brain tumor doesn't show a high disease incidence compared with other tumor types, brain and other central nervous system (CNS) tumors are indeed among the most fatal cancers and account for substantial morbidity and mortality [5]. That's mainly due to the brain and CNS play a great role in control the normal operation of human body functions. In the past years (statistics from 2008 to 2017), through the development of medical technology and the popularization of popular science knowledge, the overall malignant brain tumor incidence has become stable and even slightly declined, but incidence of children and adolescents increased 0.5% to 0.7% per year [5]. Among all of the brain tumor kinds, the glioma takes nearly more than half of the malignant ones and is famous for the infiltrative characteristics [6]. Tumor cell infiltration grows into the surrounding healthy tissue, which directly causes a dilemma about the identification of tumor boundaries during the surgery to maximize tumor excision and minimize postoperative neurological damage. In order to improve the total tumor excision precisely, some methods like image-based navigation, intraoperative sampling, electrophysiological monitoring, and enhanced visual tumor demarcation have been proposed to implement in clinical [6]. With the help of magnetic resonance imaging (MRI) is already a widely used technology in medicine, the positron emission tomography (PET) / MR neuroimaging was used for accurate delineation of glioma infiltration [7]. Even this is commonly used in the hospital, the boundary of the image is not clear. So, some image enhanced technologies are proposed to improve these methods. In 2018, Non-Sub sampled Contourlet Transform (NSCT) method was proposed to enhance the brain image and also the more representative texture features could be extracted from the enhanced brain images [8]. The efficiency has been proved on some public datasets. Besides the data transform, the pixel segmentation is also a major way to improve the image identification ability. In 2019, the adaptive superpixel generation algorithm was proposed for automatic glioma segmentation from the T2 weighted MRI [9]. It is not enough to meet the clinical practical diagnostic standards only from the perspective of improving the existing image technology, so introducing new information is an inevitable trend. For instance, the field potentials recording in the brain tissue has been proposed as a new criterion for determination of glioma boundaries [10]. Although there are many new criteria, the establishment of a clear connection between them with the physical mechanism of the tumor needs further research. Meanwhile, the equipment such as intraoperation MRI and PET are also expensive, and the maintenance consumption cannot be ignored either. Therefore, many spectral techniques have been regarded as an important prospect in this field.

The spectral techniques can provide the physical information of tumor from different perspectives. The fluorescence has been verified to be related to some specific biomarkers, for instance, 5-aminolevulinic acide induced protoporphyrin IX (PpIX) fluorescence can be applied for guiding the glioma surgery because the PpIX accumulated in normal brain cells is significantly less than in glioma cells [11]. However, there is a difference between the yellow fluorescence boundary and the actual boundary of the tumor in high-grade glioma, and the fluorescent signal will obviously weaken with the extension of the operation time [12]. Meanwhile, the novel fluorescent probe with other biomarkers cannot avoid these issues completely either [13]. The protein secondary structure can introduce different Fourier transform infrared spectroscopy (FTIR) signals, so the FTIR was also used to investigate the morphological and biochemical properties of human astrocytes, microglia, glioma cells, and glioblastoma cells [14]. Indeed, the 4 types of cells could be clearly separated with principal component analysis (PCA), but there are obvious differences in identifying the cultured pure cells and real tissues in the operation. The Raman spectroscopy peaks can directly represent the molecular bond information of the measuring sample. Due to the weak signal, the surface-enhanced Raman scattering (SERS) strategy was developed for the rapid identification of glioma boundaries [15]. The sensing chip composed of silver

nanoparticles self-assembled film was used to enhance the Raman signal. Similar to this, the nano particles enhanced technology has been also used in phototheranostic nanoprobe [16]. The phototheranostic nanoprobe enabled fluorescence, photoacoustic, and infrared thermal imaging with desirable detecting depth and high signal-to-background ratio (SBR) for differentiating brain tumors from surrounding tissues. However, the use of markers introduced exogenous substances to the human body. The impact of the exogenous and the time required for metabolism are incomplete understood. Biomarkers need a process to produce effects in the human body, and the duration will also be affected by individual differences. Based on these considerations, no marked techniques will be a trend of new diagnostic methods.

As the popular novel no exogenously marked techniques, the hyperspectral imaging (HSI) and Terahertz (THz) technologies have been conducted in the glioma boundary detection [17–19]. Due to the specific frequency, THz technology has shown great potential in molecular marker detection and can be applied in the identification of glioma boundary [17]. Nevertheless, the border of the THz imaging is still unclear, and the THz source is a bit expensive, which causes that the actual application still takes a long time. The HSI also confronts this illegibility problem of the image boundary and the relationship between HSI signal and physical chemistry mechanism is still not definite.

Compared with all these methods, laser-induced breakdown spectroscopy (LIBS) has shown potential tissue analysis ability based on advantages of the micro-damage, real-time, multi-element and molecular band analysis at the same time [20,21]. Recent years, the LIBS technique has been conducted in biomedical field like discriminating neoplastic tissues from non-neoplastic ones [22]. Based on the excellent chemical composition recognition ability, researchers have applied this technique in lung cancer [23], myeloma [24], ovarian cancer [25], parathyroid gland [26], and gastrointestinal stromal tumor [27]. Even by combining quantitative methods, the LIBS can be used to determine the content of different metal elements in nails and hair [28].

The element components of different tissues are also different, so LIBS provide a potential tumor boundary judgment method, and it has been applied for the skin tumor margin like melanoma tissue [29,30]. Since 2020, the LIBS has been proposed to detect the glioma infiltrative boundary and combined with chemometrics and machine learning methods, the LIBS have achieved significant effect on identification of glioma and boundary tissue [31–33]. However, the glioma is different from other tumors due to its infiltrative characteristics. The tumor, boundary and healthy tissues should all be identified during the surgery. Due to the different degrees of infiltration, the proportion of cancer cells and normal cells contained in the boundary tissue is also different. It is difficult to identify the tissues precisely just based on the element component reflected by LIBS spectra. Therefore, it is an inevitable trend to introduce new information dimension.

Considering the retaining element information and exploring the light polarization of induced plasma, we propose to use full-Stokes laser-induced breakdown spectroscopy (FSLIBS) method for glioma detection. The degree of polarization (DoP) has been used in the LIBS measuring techniques [34], but the DoP can only represent limited polarization information. The Stokes parameters can represent the whole polarization state of the detected light signals and carry more information to characterize the surface roughness or other features [35,36]. The Stokes features have been used in HSI techniques recent years and show its advantages to some extent [37]. In this work, the FSLIBS system is proposed to get full-Stokes information of the induced plasma. To verify the elemental composition of the glioma, boundary and healthy tissue, the inductively coupled plasma mass spectrometry (ICP-MS) and LIBS are also used during the analysis and the identification results are compared.

2. Materials and methods

2.1. FSLIBS theory

Various polarization state of monochrome plane light waves can be represented by Stokes parameters (S_0, S_1, S_2, S_3). Among them, S_0 represents total light intensity, S_1 represents the linear polarization component in horizontal direction, S_2 linear polarization component in vertical direction, S_3 represents circle polarization information in right rotation. As the Eq. (1), the relationship between the four Stokes parameters can be expressed according to the S component E_S, P component E_P, and phase difference δ of the light.

$$\begin{cases} S_0 = \left\langle E_p^2(t) \right\rangle + \left\langle E_s^2(t) \right\rangle \\ S_1 = \left\langle E_p^2(t) \right\rangle - \left\langle E_s^2(t) \right\rangle \\ S_2 = 2 \left\langle E_p(t) E_s(t) \cos \delta(t) \right\rangle \\ S_3 = 2 \left\langle E_p(t) E_s(t) \sin \delta(t) \right\rangle \end{cases} \tag{1}$$

In Eq. (1), the $E_S(t)$ reflects the timely function of S component in light, which reflects the light with the vibration direction in the incident surface. the $E_P(t)$ reflects the timely function of P component in light, which reflects the light with the vibration direction vertical to the incident surface.

It is very difficult to directly measure the phase, so the Stokes parameters are calculated by the intensity measurements. As shown in Fig. 1, by detecting the emission light modulated by a quarter-wave plate (QWP) and a polarizer, the polarization information can be demodulated.
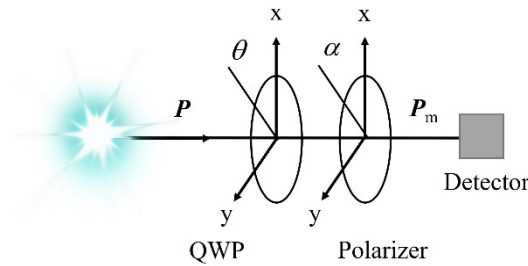

Fig. 1. The principle of Stokes parameter measurement.

The Mueller matrix reflects the integral polarization information of the light. All the waveplates can be recognized as the linear delayer, and the specific parameters depend on the crystal materials and phase delay. In order to understand the function of the QWP, the linear delayer is first

mentioned. The Mueller matrix of linear delayer is illustrated as Eq. (2),

$$
\mathbf{M_R} =
\begin{bmatrix}
1 & 0 & 0 \\
0 & \cos^2(2\theta) + \cos(\delta)\sin^2(2\theta) & \cos(2\theta)\sin(2\theta) - \cos(2\theta)\cos(\delta)\sin(2\theta) \\
0 & \cos(2\theta)\sin(2\theta) - \cos(2\theta)\cos(\delta)\sin(2\theta) & \cos(\delta)\cos^2(2\theta) + \sin^2(2\theta) \\
0 & -\sin(2\theta)\sin(\delta) & \cos(2\theta)\sin(\delta)
\end{bmatrix}
$$

$$
\begin{aligned}
&\begin{matrix}
0 \\
\sin(2\theta)\sin(\delta) \\
-\cos(2\theta)\sin(\delta) \\
\cos(\delta)
\end{matrix}
\end{aligned}
=
\begin{bmatrix}
1 & 0 & 0 & 0 \\
0 & \cos^2(2\theta) & \cos(2\theta)\sin(2\theta) & p\sin(2\theta) \\
0 & \cos(2\theta)\sin(2\theta) & \sin^2(2\theta) & -p\cos(2\theta) \\
0 & -p\sin(2\theta) & p\cos(2\theta) & 0
\end{bmatrix}
$$

$$(2)$$

where the δ represents the phase delay and p is a related numerical parameter (the value is 1 and the sign depends on the crystal material). As a positive crystal, the δ of QWP used in this work is $-\pi/2$, and p is -1. The θ ($0° \leq \theta \leq 180°$) is the fast axis angle, which represents the angle between the fast axis of QWP and the x-axis. The Mueller matrix of QWP is shown as Eq. (3) and the polarizer one is shown as Eq. (4),

$$
\mathbf{M_{QWP}} =
\begin{bmatrix}
1 & 0 & 0 & 0 \\
0 & \cos^2(2\theta) & \cos(2\theta)\sin(2\theta) & -\sin(2\theta) \\
0 & \cos(2\theta)\sin(2\theta) & \sin^2(2\theta) & \cos(2\theta) \\
0 & \sin(2\theta) & -\cos(2\theta) & 0
\end{bmatrix}
\tag{3}
$$

$$
\mathbf{M_{LP}} = \frac{1}{2}
\begin{bmatrix}
1 & \cos(2\alpha) & \sin(2\alpha) & 0 \\
\cos(2\alpha) & \cos^2(2\alpha) & \cos(2\alpha)\sin(2\alpha) & 0 \\
\sin(2\alpha) & \cos(2\alpha)\sin(2\alpha) & \sin^2(2\alpha) & 0 \\
0 & 0 & 0 & 0
\end{bmatrix}
\tag{4}
$$

where the α ($0° \leq \alpha \leq 180°$) represents the angle between the transmitted axis of the polarizer and the vertical direction. The combined Mueller matrix of the system is as Eq. (5).

$$\mathbf{M}_{(\alpha,\theta)} = \mathbf{M}_{\text{LP}} \times \mathbf{M}_{\text{QWP}} = \tfrac{1}{2}
\begin{bmatrix}
1 \\
\cos(2\alpha) \\
\sin(2\alpha) \\
0
\end{bmatrix}$$

$$\cos(2\alpha)\cos^2(2\theta) + \sin(2\alpha)\cos(2\theta)\sin(2\theta)$$
$$\cos^2(2\alpha)\cos^2(2\theta) + \cos(2\alpha)\sin(2\alpha)\cos(2\theta)\sin(2\theta)$$
$$\cos(2\alpha)\sin(2\alpha)\cos^2(2\theta) + \sin^2(2\alpha)\cos(2\theta)\sin(2\theta)$$
$$0$$

$$\cos(2\alpha)\cos(2\theta)\sin(2\theta) + \sin(2\alpha)\sin^2(2\theta)$$
$$\cos^2(2\alpha)\cos(2\theta)\sin(2\theta) + \cos(2\alpha)\sin(2\alpha)\sin^2(2\theta)$$
$$\cos(2\alpha)\sin(2\alpha)\cos(2\theta)\sin(2\theta) + \sin^2(2\alpha)\sin^2(2\theta)$$
$$0$$

$$-\cos(2\alpha)\sin(2\theta) + \sin(2\alpha)\cos(2\theta)$$
$$\cos(2\alpha)\sin(2\alpha)\cos(2\theta) - \cos^2(2\alpha)\sin(2\theta)$$
$$\sin^2(2\alpha)\cos(2\theta) - \cos(2\alpha)\sin(2\alpha)\sin(2\theta)$$
$$0$$

$$\tag{5}$$

Given the incident light vector of Stokes parameters as Eq. (6), the modulated light will be as Eq. (7).

$$\boldsymbol{P} = (S_0, S_1, S_2, S_3)^{\text{T}} \tag{6}$$

$$\boldsymbol{P}_{\text{m}} = \mathbf{M}_{\text{LP}} \times \mathbf{M}_{\text{QWP}} \times \boldsymbol{P} = \mathbf{M}_{\text{total}} \times \boldsymbol{P} \tag{7}$$

Adjusting the angles of QWP and polarizer, the Mueller matrixes of four sets of angles are illustrated as Eq. (8)–(11).

$$\mathbf{M}_{(0°,45°)} =
\begin{bmatrix}
0.5 & 0 & 0 & 0.5 \\
0 & 0 & 0 & 0 \\
0.5 & 0 & 0 & 0.5 \\
0 & 0 & 0 & 0
\end{bmatrix} \tag{8}$$

$$\mathbf{M}_{(0°,135°)} =
\begin{bmatrix}
0.5 & 0 & 0 & -0.5 \\
0 & 0 & 0 & 0 \\
-0.5 & 0 & 0 & 0.5 \\
0 & 0 & 0 & 0
\end{bmatrix} \tag{9}$$

$$\mathbf{M}_{(0°,0°)} = \begin{bmatrix} 0.5 & 0.5 & 0 & 0 \\ 0.5 & 0.5 & 0 & 0 \\ 0 & 0 & 0 & 0 \\ 0 & 0 & 0 & 0 \end{bmatrix} \tag{10}$$

$$\mathbf{M}_{(45°,45°)} = \begin{bmatrix} 0.5 & 0 & 0.5 & 0 \\ 0 & 0 & 0 & 0 \\ 0.5 & 0 & 0.5 & 0 \\ 0 & 0 & 0 & 0 \end{bmatrix} \tag{11}$$

Based on these Mueller matrixes, the Stokes parameters can be calculated as Eq. (12).

$$\begin{cases} S_0 = I(0°, 45°) + I(0°, 135°) \\ S_1 = 2I(0°, 0°) - (I(0°, 45°) + I(0°, 135°)) \\ S_2 = 2I(45°, 45°) - (I(0°, 45°) + I(0°, 135°)) \\ S_3 = I(0°, 45°) - I(0°, 135°) \end{cases} \tag{12}$$

2.2. FSLIBS experimental measuring setup

Based on the theory in Section 2.1, the FSLIBS setup for glioma samples detection is illustrated in Fig. 2. Among the system, a flash-pumped Q-switched Nd: YAG laser (1064 nm, 1 Hz, $\tau = 5$ ns, Ø6 mm, optimized to 30 mJ/pulse) is used to excite the tissues. Considering the inconvenience brought by the invisible infrared laser, a He-Ne laser ($\lambda = 632.8$ nm) is used as pointing laser to calibrate the optical path. To optimize the experimental parameters, the laser energy is adjusted by a half-wave plate (HWP) and a polarization prism. Then, the pulse energy is monitored by an energy meter (PE50BF-C, Starlite, Ophir). During the experiments, the fluctuation of the laser energy is less than 2%. The laser propagation direction is changed through three reflected mirrors and finally focused on the sample surface by a 10× near-infrared correction objective (M Plan Apo NIR, Mitutoyu).
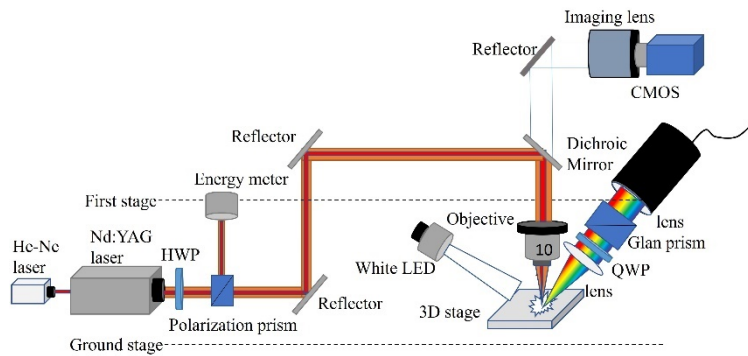

Fig. 2. Schematic of the FSLIBS experimental setup.

Then for the spectral collection part, the plasma radiation is collected by two convex lens (focus length: 75 mm and 50 mm) and transfer into a two-channel fiber spectrometer (AvaSpec

2048-2-USB2, Avantes, 190~1100 nm, 0.2~0.3 nm). A superachromatic QWP (SAQWP05M-700, Thorlabs, 325~1100 nm) and a Glan prism (GCL-070214, Daheng Optics, 220~2500 nm) are added between the two lenses to modulate the plasma spectra. A COMS camera (ME2L-161-61U3M, Daheng Imaging) is used to observe the focus point on the sample and the white LED provides a bright vision. External trigger used in the system include a photodetector and a digital delayer (SRS-DG535, Stanford Research System). The spectrometer is triggered by DG535 after a preset delay time. In order to achieve a good signal-to-background ratio, the spectral acquisition delay time and the integration time are optimized to 1.29 µs and 2 ms.

2.3. Glioma samples detection

In this work, glioma, boundary, and healthy tissues were obtained from department of neuro-oncology of the hospital after routine tumor surgery. The study was approved by the ethics committee at the Kunming Sanbo Brain Hospital (Kunming, China, April 2020). Due to the samples we used are all high-grade gliomas, the removal area has been expanded to a certain extent to avoid recurrence. So, a little normal tissue can be collected. The 36 samples were collected from 6 patients (18 for the LIBS and 18 for the FSLIBS detection) and the specific information as listed in Table 1. Both routine pathological diagnosis and molecular gene diagnosis were conducted to the corresponding samples from these patients and made sure the accurate prior diagnostic results as glioma.

Table 1. The information of patients and samples for the LIBS and FSLIBS detection

Sample Index	Pathological attribute	Patient index	Gender	Age
1, 19	Healthy			
2, 20	Boundary	1	Female	47
3, 21	Glioma			
4, 22	Healthy			
5, 23	Boundary	2	Male	56
6, 24	Glioma			
7, 25	Healthy			
8, 26	Boundary	3	Female	62
9, 27	Glioma			
10, 28	Healthy			
11, 29	Boundary	4	Male	25
12, 30	Glioma			
13, 31	Healthy			
14, 32	Boundary	5	Male	36
15, 33	Glioma			
16, 34	Healthy			
17, 35	Boundary	6	Male	15
18, 36	Glioma			

All the samples were preserved at -80°C after the surgery until the LIBS measurement. The main difference between LIBS biological tissue measurement and conventional hard sample detection is the sample form. Due to the soft texture and the residue of blood and tissue liquid on the surface, the laser energy is difficult to be coupled for exciting the tissue sample. The liquid will also absorb heat and cause the temperature of the plasma to decrease, resulting in weak spectral signals. Therefore, the samples were put on the glass slides and were blew by the heat wind for 5 seconds from a distance at 25 cm. The representative samples were shown as Fig. 3.

Due to the different size of each tumor, the number of spectra available for each tumor was also different. Every spectrum was detected at a new spot and after filtering the spectra ablated the substrate, the LIBS spectra and FSLIBS spectra were used for the following analysis.
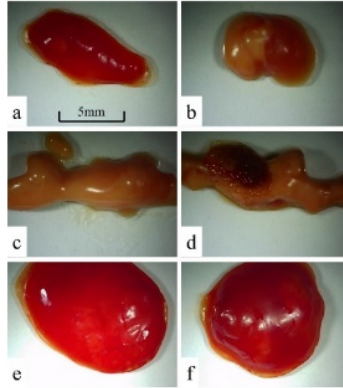

Fig. 3. The representative samples of patient 1 (a: healthy, c: boundary, e: glioma) and patient 2 (b: healthy, d: boundary, f: glioma).

In order to verify the elemental composition of the glioma and related tissues, another 6 samples were collected from the patient 1 and 2 for the ICP-MS measurement. A commercial ICP-MS system (ICP-MS 7800, Agilent) was used for the detection. The samples were digested for the analysis and the information were listed in Table 2.

Table 2. The information of samples for ICP-MS measurement

Index	Sample	Digestion volume(mL)	Sample mass(g)
1	Patient 1 healthy	10	0.1137
2	Patient 1 boundary	10	0.3574
3	Patient 1 glioma	10	0.4011
4	Patient 2 healthy	10	0.1092
5	Patient 2 boundary	10	0.1262
6	Patient 2 glioma	10	0.3409

3.   Results and discussion

3.1.   ICP-MS elemental analysis of glioma

The ICP-MS scanned 65 kinds of elements during the detection, and the detection contents of the main elements (content > 0.1 mg/kg) were listed in the Table 3. Take an example, the elemental composition of sample 1 is shown in the Fig. 4. Because mass spectrometry detection methods cannot measure the main components of organic elements like C, H, O, etc., the non-metallic element P expressed the highest content as an important component of organic element in organisms such as protein and phospholipids. The following high content is Na and K elements that have important regulatory effects on the infiltration balance and acid-base balance in the body. This result is consistent with the prior knowledge of biology, so the detection results of ICP-MS can be used to verify the content of glioma and related tissues.

The Table 3 illustrated 4 kinds of non-metallic elements (B, Si, P, Se) and 12 kinds of metal elements (Na, Mg, Al, K, Ca, Ti, Cr, Mn, Fe, Cu, Zn, Rb). The comparisons between two patients in non-metallic and metal elements are shown in Fig. 5 and Fig. 6, respectively.

Table 3. The main elements and contents of 6 samples detected by ICP-MS[a]

Elemental content	Sample 1	Sample 2	Sample 3	Sample 4	Sample 5	Sample 6
B (mg/kg)	0.4559	0.1705	0.1359	0.4523	0.3882	0.1322
Na (mg/kg)	2201.2397	1872.0753	2674.3452	2792.7722	2828.8006	2838.1862
Na[He] (mg/kg)	1976.7608	1729.7505	2318.9342	2518.0385	2464.8970	2431.5551
Mg (mg/kg)	97.6021	163.7647	116.6566	145.9745	115.4270	103.5068
Al (mg/kg)	2.5203	0.7745	2.2756	2.9471	2.6110	0.7720
Si (mg/kg)	20.4042	10.6644	12.6464	40.2759	35.4712	13.9727
P (mg/kg)	2326.3988	5317.0617	2856.3578	3799.9448	3610.7830	1996.7571
K (mg/kg)	1651.8313	2604.8627	1784.4184	2176.9431	1134.8757	1664.3606
Ca (mg/kg)	53.5636	72.8805	109.0821	82.7004	75.9163	206.2334
Ti (mg/kg)	0.8287	1.7082	0.9326	1.3213	1.2449	0.6307
Cr (mg/kg)	0.6533	0.5125	0.4950	0.9872	0.8229	0.4319
Mn (mg/kg)	0.2990	0.3569	0.5905	0.4593	0.3902	0.4027
Fe (mg/kg)	65.9780	63.4802	170.7352	90.7354	65.0089	515.0495
Cu (mg/kg)	5.4053	4.9431	3.2218	5.8527	3.8914	3.5088
Zn (mg/kg)	9.2308	8.9996	9.0796	12.9086	7.3278	14.7785
Se[He] (mg/kg)	0.1284	0.1353	0.1429	0.1955	0.1136	0.1880
Rb (mg/kg)	2.0961	3.8054	3.4992	2.8844	1.9147	3.3745

[a][He]: The measurement in the helium atmosphere. Other measurements are in the vacuum.

Among the non-metallic elements, B shows the same changing trends in the two patients for the three kinds of tissues. From normal tissue to tumor tissue, the content shows a trend of decrease. But in general, the content of B in the human body is relatively low, and the concentration of all samples does not exceed 0.5 mg/kg. For Si, the content of tumor areas is lower than normal tissue, but the content of boundary tissue is unstable. It is difficult to identify the tumor boundary according to Si. Because the infiltration characteristics of glioma are slightly different due to the specific growth of the tumor, the infiltration ratio of cancer cells in the different tumors and even different positions of the same tumor may be different. This may also be one of the reasons for the unstable elemental content. The P content is extremely high, which is mainly related to its participation in the phosphate buffer mechanism in the blood [38]. As a result of this, bleeding
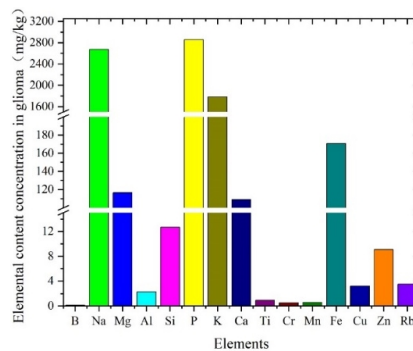
Fig. 4. The main elements and contents of glioma scanned by the ICP-MS.
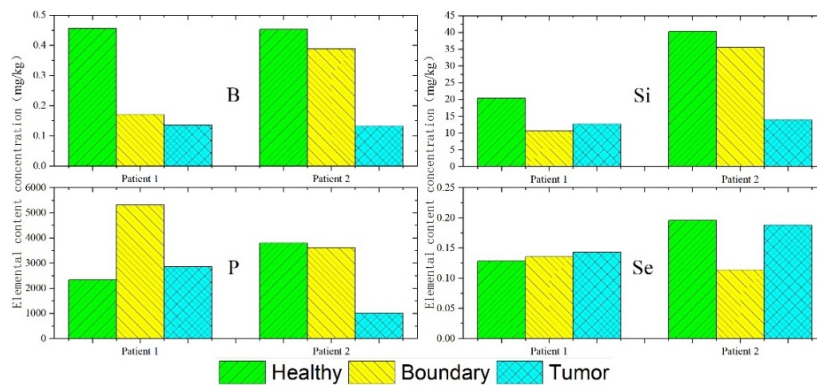
Fig. 5. The main non-metallic elements content comparison in patient 1 and 2 (B, Si, P, Se).
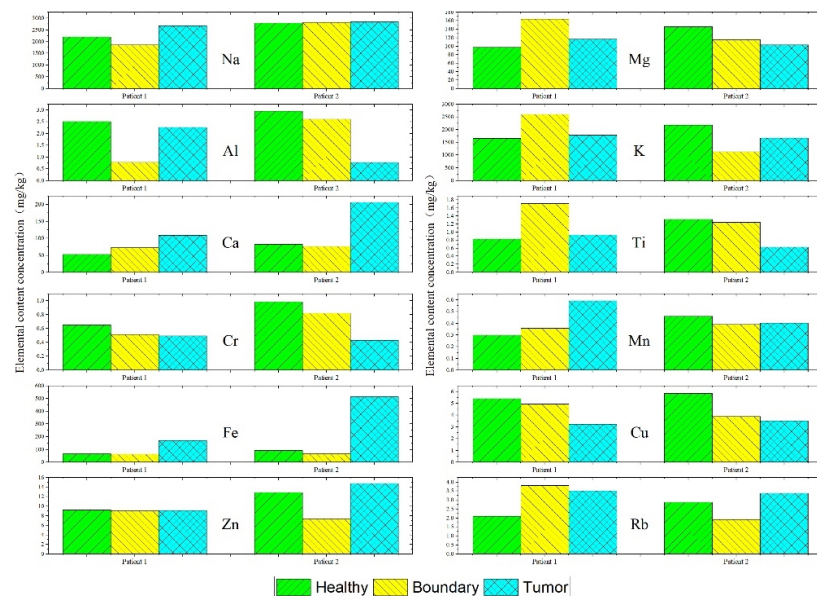

Fig. 6. The main metal elements content comparison in patient 1 and 2 (Na, Mg, Al, K, Ca, Ti, Cr, Mn, Fe, Cu, Zn, Rb).

during the operation and exudation of tissue fluid will both have important impacts on the content of the P element. The Se also doesn't show an obvious trend.

Among the metal elements, Na, Mg, K, Ca, and Fe are common elements in biological tissues. The Cr and Cu contents in the three types of tissues of the two patients are relatively consistent. From normal tissue to tumor tissue, the contents of both elements show a decreasing trend. The Cu participates in the synthesis of many enzymes in the human body and acts as an important component of the brain neurotransmitters [39]. The lack of Cu will lead to reduced pigment oxidase in the brain cells. In severe cases, it may even lead to symptoms such as unstable gait. Some glioma patients also show similar symptoms to a certain extent, which can speculate that the glioma may cause the Cu content level to decrease in the lesion. Although Cr is an important trace element of the human body, the overall content is extremely low, and the measurement bias may cause the trend between the two patients not universal. The Fe ions are the main hematopoietic raw material in the human body, and it is also the main component of hemoglobin. The growth of cells in the tumor area requires more nutrients and requires more blood supply, so the amount of Fe will also increase [40]. The Ca content in the tumor area is higher than the normal brain tissue area, which is consistent with the calcification phenomenon that occurs in many tumors [33]. The Na and K contents are extremely rich, but at the same time, it is also susceptible to interfering blood and interstitial fluid [38]. Different osmotic pressure will also affect the flow direction of the interstitial fluid. Although we do not have a good consistency ICP-MS conclusion on Na or K here, it is undeniable that as a rich metal element, it may still play an important role in the diagnosis. In order to further analyze the relationship between different elements, the measured elemental concentration is compared with each other, and the concentration rate with the same trend between two patients is listed in Table 4. Among them, 8 groups are related to Ca. Although the standards of tissue elements difference cannot be summarized from the consistency of the two patients, the Ca is still an important element that characterizes the differences in glioma boundary.

Table 4. The concentration ratio with the same trend between two patients.

Index	Elemental rate	Index	Elemental rate	Index	Elemental rate
1	B:Na	11	P:Ca	21	Ti:Cr
2	B:Si	12	P:Mn	22	Ti:Mn
3	B:Ca	13	P:Fe	23	Ti:Fe
4	Na:Si	14	P:Rb	24	Ti:Rb
5	Na:Ti	15	K:Rb	25	Cr:Mn
6	Na:Cr	16	Ca:Ti	26	Mn:Fe
7	Mg:Ti	17	Ca:Cr	27	Mn:Cu
8	Mg:Fe	18	Ca:Fe	28	Fe:Cu
9	Al:P	19	Ca:Cu	29	Zn:Rb
10	Si:Ca	20	Ca:Zn		

3.2. LIBS elemental and molecular analysis of glioma

The LIBS spectra of the corresponding samples from patients 1 and 2 are shown in Fig. 7. Although there are large differences in the whole spectra of same tissues from these two representative patients, some spectral peaks maintain stability. We can recognize 13 elemental peaks of 6 elements, which are listed in Table 5. In all tissues, the intensities of Na peaks are obviously high, which is consistent with the prior knowledge of Na maintained the infiltration balance in the body and the ICP-MS detection results. In these examples, the Ca intensities are significantly weaker in boundary tissues than tumor and normal tissues. Meanwhile, multiple

spectral lines corresponding to each element may be seen in the LIBS spectrum. Therefore, different spectral lines of the same element should be analyzed separately. In tumor tissue, the proportion of Na and K intensities has maintained better consistency, forming a certain difference with healthy and boundary tissues. In order to further analyze the relationship between different elemental lines, the measured line intensity is compared one by one, and the intensity rate with the same trend between two patients is listed in Table 6. All the four sets of rates are related to Ca and Na. Although the element of consistency is different with ICP-MS, they both shows the important role of Ca in characterizing the tissue. Since the sample is consumable in the detection, ICP-MS detection and LIBS detection have not analyzed the same sample. But the sample originated from the same operations of the same patients.
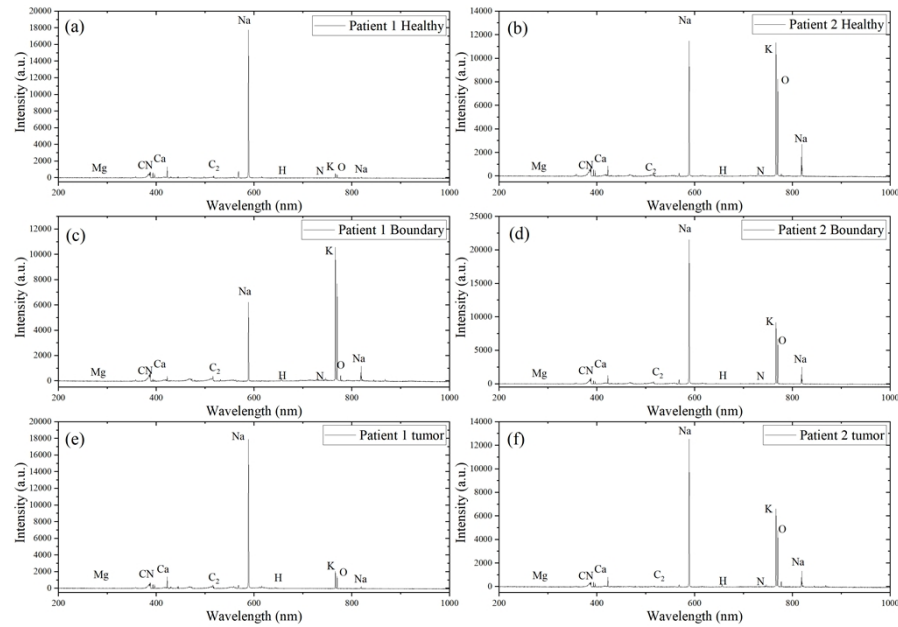

Fig. 7. The averaged LIBS spectra of different tissues from patient 1 and 2.

Table 5. The LIBS elemental lines and corresponding wavelengths.

Elements	Wavelengths (nm)
Mg	279.1, 279.8
Ca	393.4, 396.8, 422.7
Na	589.0, 589.6, 818.3, 819.5
H	656.3
K	766.5, 769.9
O	777.4

In the LIBS detection, in addition to the elemental lines of atoms and ions, there are also some molecular fragmental bands that cannot be ignored. The molecular bands have been used in the LIBS analysis and been considered as reliable biological tissue detection marks [32,33]. As the detection spectra shown in Fig. 7, the CN and C_2 bands also appeared. The measured LIBS molecular bands are listed in Table 7. Experiments are performed in the atmospheric

Table 6. The LIBS elemental line rates with the same trend between two patients.

Index	LIBS elemental line rate
1	Ca (393.4 nm) : Na (589.0 nm)
2	Ca (396.8 nm) : Na (589.0 nm)
3	Ca (393.4 nm) : Na (589.6 nm)
4	Ca (396.8 nm) : Na (589.6 nm)

environment, so the measured C and N elements may not only come from the sample, but also may be derived from the environmental atmosphere.

Table 7. The LIBS molecular bands and corresponding wavelengths

Molecular band	Central wavelength (nm)	Containing lines (nm)
CN(1,0)	358.4	358.4
CN(0,0)	384.0	384.6, 385.7, 386.5, 388.0
$C_2(0,0)$	516.8	516.8, 517.9
$C_2(0,1)$	558.5	558.5

The C in the air mainly comes from the weak CO_2 content (0.03%~0.04%). The content proportion is extremely low, and the contribution to the spectral signal is weak. Relatively speaking, the N element is high in the air, and it does contribute to the ingredients in the CN bands, but the nitrogen content in the atmosphere is relatively stable, and the impact on different samples is relatively uniform. Therefore, the molecular bands can still reflect the composition and the interaction between the sample and laser [41]. The intensities of the molecular bands are lower than that of the rich metal elemental spectral lines, and the measured fluctuation is large. Among the 3 kinds of tissues from the two patients, there's no consistency trend in single molecular band. Therefore, compared the intensity of 8 lines in these bands one by one, all ratios with consistent trends are listed in Table 8. Although the consistency showing between two patients cannot be used as the standard for tissue identification, to a certain extent, it has proved that the CN and C_2 molecular bands may provide a basis for glioma boundary identification.

Table 8. The LIBS molecular band line rates with the same trend between two patients

Index	LIBS molecular band line rate
1	CN (358.4 nm):C_2 (558.5 nm)
2	CN (384.6 nm):CN (388.0 nm)
3	CN (384.6 nm):C_2 (517.9 nm)
4	CN (385.7 nm):CN (388.0 nm)
5	CN (385.7 nm):C_2 (517.9 nm)
6	CN (386.5 nm):C_2 (517.9 nm)
7	CN (388.0 nm):C_2 (517.9 nm)

For the LIBS measurements, the spectral numbers collected from 18 samples are listed in Table 9. The spectral data from each patient has a certain fluctuation. There are two main reasons for the differences in line intensity and data distribution of these tissues. The first one is the individual differences of each patient cause the difference in tissue components not only related to the tumor, but also affected by the patient's habits. The other one is heterogeneity of the tumor tissue, so the tissue sample parts for pathological detection and LIBS detection

has a slight difference in malignant ratio [42]. Therefore, direct identification from the spectra is significantly difficult. The machine learning methods have been used in the pathological diagnosis recent years and perform well-known ability [43,44]. We applied several machine learning and deep learning methods for the glioma LIBS spectra identification. For instance, *k*-nearest neighbor (*k*-NN), support vector machine (SVM), soft independent modeling class analog (SIMCA), random forests (RF), artificial neural networks (ANN), and spiking neural network (SNN). In order to ensure the training of the model, only 3 samples from one patient (patient 4) were selected as the source of the testing set due to the small number of patients, and the samples of other five patients were used as the source of the training set. The identification accuracies are shown in Fig. 8.
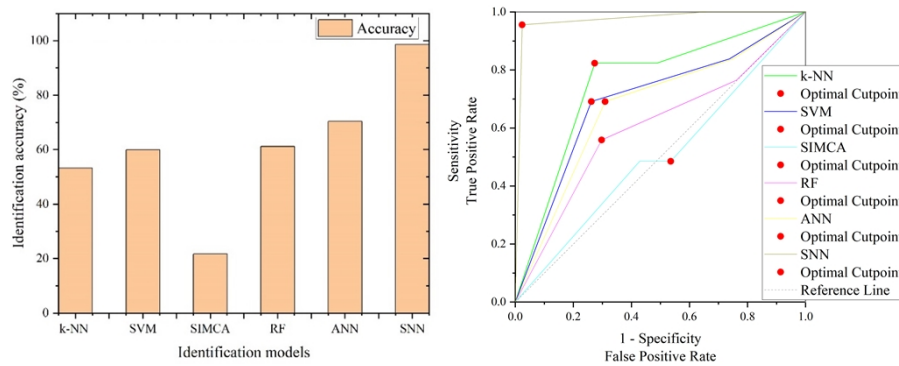

Fig. 8. The identification accuracies and ROC curves of different models.

Table 9. The number of LIBS spectra collected from 18 samples

Sample index	Spectral number	Sample index	Spectral number	Sample index	Spectral number
1	63	7	60	13	39
2	47	8	59	14	52
3	59	9	54	15	47
4	64	10	29	16	52
5	66	11	55	17	44
6	68	12	68	18	46

The identification accuracies of neural network models are better than other models with LIBS spectral features. Especially the SNN model, even achieved the accuracy of 98.68%. This is mainly due to large data fluctuations hinder the ability to learn effective data characteristics of the traditional machine learning models. However, during an in-depth investigation of SNN, it is found that the accuracy of training set is low, only about 60%. This is due to the large differences in the training set data itself. In the pulse training process of SNN, data relationship is not fully learnt and instead the overfitting phenomenon is avoided. The receiver operating characteristic (ROC) curves are also showed in Fig. 8. For the six kinds of the identification models (*k*-NN, SVM, SIMCA, RF, ANN and SNN), the area under the curve (AUC) values are 0.75595, 0.69538, 0.50079, 0.60049, 0.67358 and 0.97365, respectively. Balanced training is a major advantage of the SNN model, but the large deviation also indicates that the model training is incomplete. Although the AUC of SNN is high, considering the predictive difference between training and test sets, the model is not trained completely. So, the high accuracy of the test data prediction is some kind of accidental phenomenon. Therefore, it can't be said that LIBS has achieved great identification effects in a strict sense, and still new information needs to be introduced.

3.3. FSLIBS analysis of glioma

The 18 samples from the same 6 patients were collected for the FSLIBS measurement. Four measurements are needed to be conducted to demodulated Stokes parameter spectra, but during the LIBS detection process, it is difficult to guarantee that each excitation is exactly the same. Therefore, to ensure that the accuracy of the demodulation is as high as possible, the similarities of the measurement spectra need to be improved. For the set of four modulation angles, 100 spectra were measured for each sample, and the most similar 50 items are selected as the spectra at the set of modulation. The Stokes parameter spectra can be calculated by Eq. (12) based on the four measurement spectra at these modulated angles. The average spectra of the FSLIBS of the healthy tissue, boundary tissue and glioma tissue are shown in Fig. 9, Fig. 10, and Fig. 11, respectively. S_0 stands for intensity information of light, and its spectral lines are also highly similar to the intensity spectra measured directly. The values of the three parameters of S_1, S_2, and S_3 are significantly smaller than the intensity information, which is consistent with the results of theoretical calculation analysis. The influence of different modulation angles on the amplitude of the intensity fluctuations of the measuring spectrum is not very large. Therefore, through the reduction between the two measurement spectra, the generated difference spectral intensity will become significantly smaller in terms of value. Most of the FSLIBS lines are still corresponding to the LIBS lines, but indeed a small number of new spectral peaks appear at different wavelengths from the original lines. This is due to the details not reflected during the intensity measurement will be enlarged in the differential spectra. In addition, the differential spectra contain both positive and negative peaks due to the subtraction process.
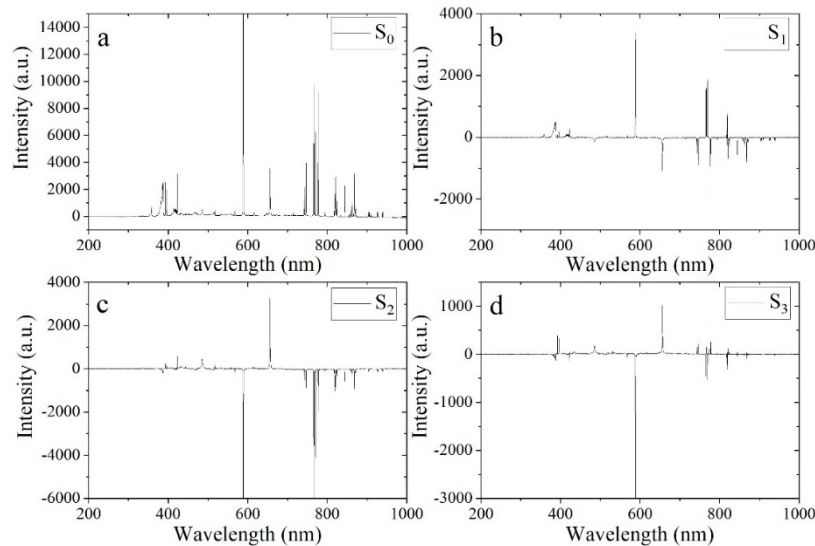

Fig. 9. The average FSLIBS spectra of healthy tissue.

Compared with healthy tissue, the intensity information S_0 of the boundary tissue does not show obvious differences, but some of the peak differences in the other three parameters are obvious. For example, in the S_1 parameter spectrum, the calculated value at Na I 589.0 nm changes to negative, which may can supplement important difference information for the identification process. The average FSLIBS spectra of the glioma tissue is different from the previous two kinds of tissues. Although the intensity signal S_0 is extremely similar, the S_1 parameter does not show negative spectral peaks, which basically maintains the shape of the original LIBS spectra. Meanwhile, even though the intensity of the S_1 lines is significantly weaker than the S_0 lines, the
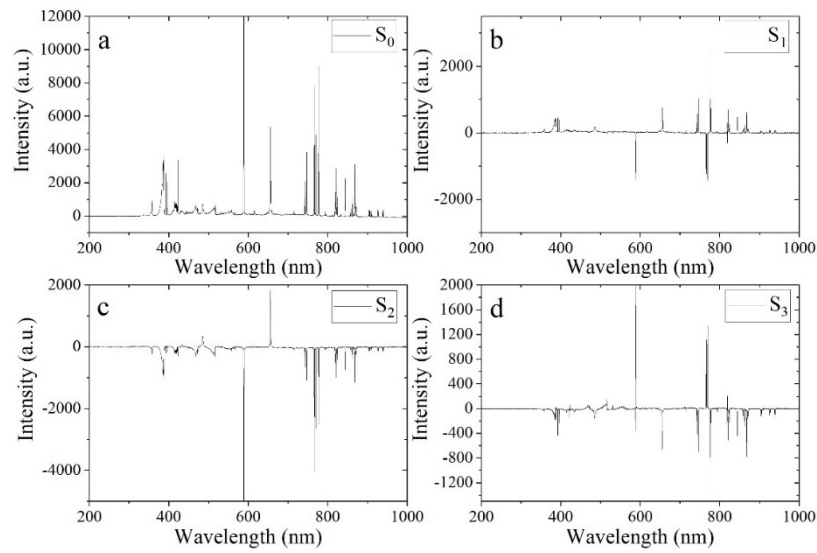
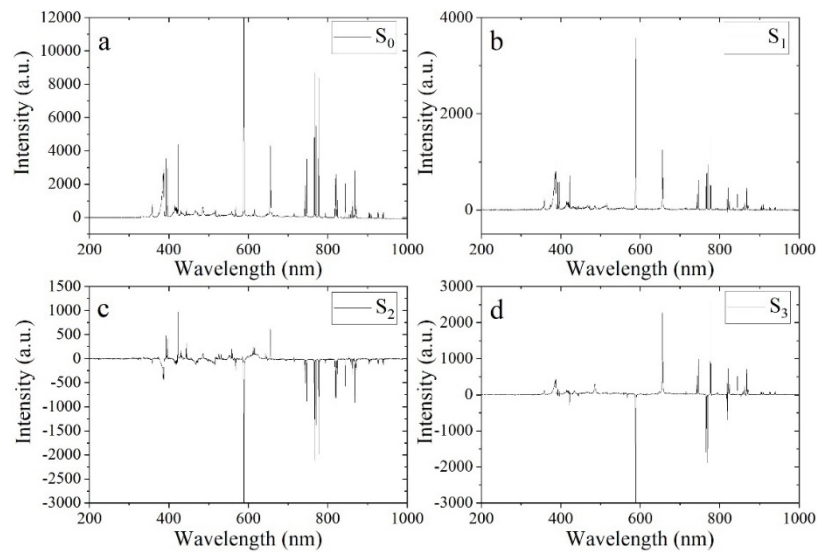**Fig. 10.** The average FSLIBS spectra of boundary tissue.

Fig. 11. The average FSLIBS spectra of glioma tissue.

SBR has not weakened significantly. This indicates that the trend of each spectral line intensity between the two measurements that are used for the subtraction is unified. However, the difference between a small number of spectral lines cannot be used directly as a basis for identification. Through the subtraction, the value order of the last three parameters obtained is significantly reduced compared with the measured spectral intensity, and the random fluctuations that show in intensity may be relatively amplified. Therefore, the differences and stability both need to be considered in FSLIBS spectra. The numbers of spectral lines identified in the four parameter spectra of S_0, S_1, S_2, and S_3 are different, including 52, 39, 43, and 34 peaks, respectively. Using the same identification models as Section 3.2, the highest accuracy achieved 65.33% with S_0 spectra and the SNN model. The accuracies of S_1, S_2, and S_3 spectra and the SNN model are 52.00%, 55.33%, and 56.00%, respectively. Although the identification accuracy is decreased compared with the LIBS intensity spectra, the accuracy of the training set and the test set is relatively balanced. The S_0 spectra and the original LIBS spectra both reflect the intensity information, but the process of multiple measurement and demodulation calculation introduces some fluctuations, making the difference of data distribution between the training set and the test set smaller.

Besides the identification, the unsupervised clustering method K-means is introduced for the analysis of FSLIBS spectra. The clustering results of FSLIBS spectra are shown in Fig. 12. For all four parameter spectra, the healthy and boundary tissues are distributed in all three predicted categories. Although the difference in axonal density and protein/lipid ratio has been proved in glioma, infiltrative and healthy brain tissue [45], the low proportion of cancer cells contained in the boundary tissue makes the difference of overall component between the health and boundary tissue is not large enough to distinguish. Meanwhile, due to individual difference of patients in the non-lesion area, the distribution of these two kinds of tissue doesn't have regular pattern, which make it cover all the predicted types. In the S_0, S_1, and S_3 parameter spectra, nearly all the glioma samples are clustered into one class. It reflects that the FSLIBS spectral difference within glioma samples is relatively small. Tumor is the main cause of changes in the elemental composition of the lesion region [22]. The influence of glioma on tissue composition is more obvious than internal differences between different patients.. Furthermore, the clustering results of glioma samples based on S_0 and S_3 parameter spectra are coincidentally just the opposite. In the S_3 spectrum, the value of specific lines at around 422 nm, 589 nm, 769 nm and other wavelengths are negative, but the trend of the absolute value among these lines is similar. These spectral lines are related to Ca, Na and K elements and act an important role in the identification. The change of these key spectral lines may be the main reason for the exchange of predicted labels. Comparing the S_1 and S_2 parameter spectra, the clustering results are more dispersed, especially for the S_2 parameter. This indicates that the spectral information in the two different linear polarization parameters has great randomness. The polarization of spectral lines is independent of the polarization direction of laser. The randomness of the linear polarization direction is more obvious than the linear polarization degree. Oppositely, the trend of circular polarization information at the key spectral lines are the same as the spectral intensity changing trends. In the laser-induced plasma, even the spectral lines of the same element, the polarization status of the lines generated between different energy levels of transition is different [46]. This is also reflected in the detected circular polarization spectral information and the circular polarization information is more dominant in the entire spectral polarization information. Furthermore, the polarization state is also directly related to the position of the detection focus distance and further experimental research is needed in this field.

Although the tumor cannot be completely identified, in contrast, the similarity within the glioma category can be characterized. In the future, the FSLIBS may can be used for the precisely identification of glioma boundary based on the characterizing ability of plasma polarizing information.
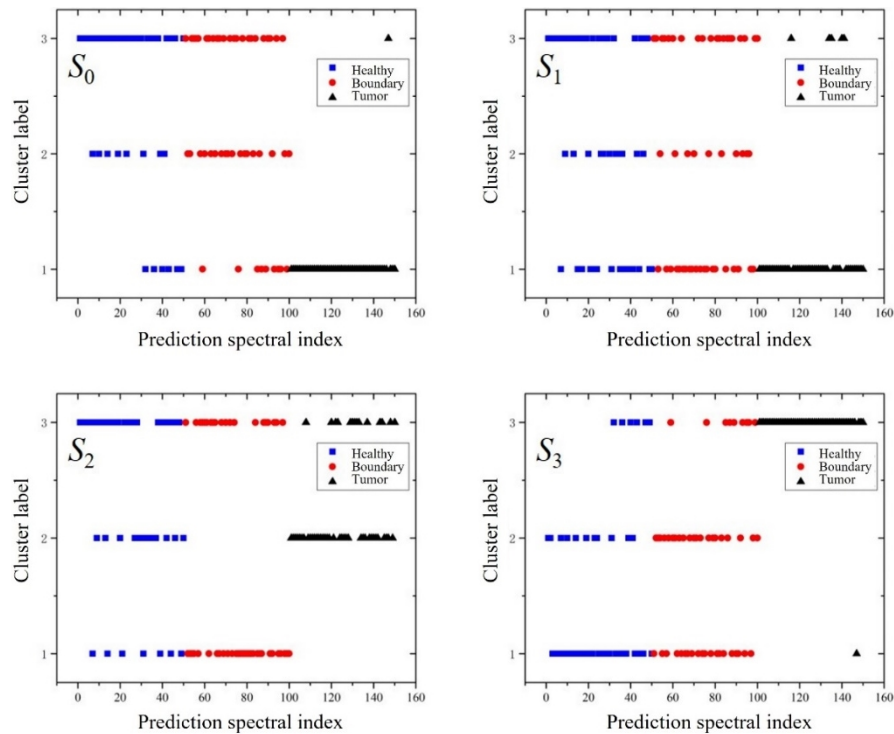
Fig. 12. The clustering results of FSLIBS spectra.

For the FSLIBS system, both the light intensity information and polarized phase information can be characterized. The intensity signal reflects the elemental composition content, and the polarization signal reflects the surface texture of the sample. Based on the preliminary conclusion, the polarization information is much stable in the tumor. Combined with the polarization information, the under-fitting phenomenon of the identification models can be solved to some extent. However, not all the samples will have stable polarization signal, sometimes it may cause the bias influence on the identification model and more experiments need to be carried out to verify the phenomenon.

For the standard LIBS technique, only the intensity information of the plasma emission can be detected. The less information can be obtained. Therefore, the detected LIBS signal is much stable, as no calculation process are needed.

4.   Conclusions

In this paper, we built a FSLIBS system for the modulation and demodulation of full-Stokes parameters in laser-induced plasma and applied for the biomedical tissue measurement. The elemental information and full-Stokes polarization information are combined in the FSLIBS signals and shows a potential ability to characterize the glioma lesion tissue. In order to verify the elemental composition of glioma and corresponding boundary and healthy tissue, the ICP-MS was used for analysis. Combined with the LIBS elemental and molecular fragmental analysis, the Ca, Na, K lines and CN, C_2 bands are recognized as important features for the identification in LIBS. The FSLIBS further introduces some other subtle peaks not appeared in the intensity spectra. The FSLIBS spectra haven't shown obvious improvement on the identification accuracy, but it can indeed reduce the under-fitting phenomenon of the identification models. It can be seen

from the unsupervised cluster labels that the clusters of the glioma are relatively stable, while the other two kinds of tissue distributions are scattered. The FSLIBS reveals that the polarization characteristics of the laser-induced glioma plasma may be relatively stable.

Meanwhile, although the Stokes parameters show the potential ability of increasing spectral differences, there is still a certain gap of FSLIBS from the application. The demodulation process of the four measurements is highly rely on the stability of the plasma emission, but due to the unevenness of the sample components and the fluctuation of laser pulse energy, it is difficult to avoid the fluctuation of the FSLIBS spectra. Although the effects of fluctuations have been weakened to a certain extent through spectral similarity filtering, more comprehensive measures are still needed to solve this problem. In addition, although the polarization mechanism in previous experience is considered to be related to the Fresnel reflection, the relationship between polarization mechanism and sample surface characteristics and the differences of polarization characteristics in each spectral peak need to be further clarified.

Disclosures. The authors declare no conflicts of interest.

Data availability. Data underlying the results presented in this paper are not publicly available at this time but may be obtained from the corresponding author upon reasonable request.

Supplemental document. See Supplement 1 for supporting content.

References

1. F. Islami, C. E. Guerra, A. Minihan, K. R. Yabroff, S. A. Fedewa, K. Sloan, T. L. Wiedt, B. Thomson, R. L. Siegel, N. Nargis, R. A. Winn, L. Lacasse, L. Makaroff, E. C. Daniels, A. V. Patel, W. G. Cance, and A. Jemal, "American Cancer Society's report on the status of cancer disparities in the United States, 2021," CA Cancer J. Clin. **72**(2), 112–143 (2022).
2. R. L. Siegel, K. D. Miller, H. E. Fuchs, and A. Jemal, "Cancer statistics, 2022," CA Cancer J. Clin. **72**(1), 7–33 (2022).
3. A. N. Giaquinto, K. D. Miller, K. Y. Tossas, R. A. Winn, A. Jemal, and R. L. Siegel, "Cancer statistics for African American/Black People 2022," CA Cancer J. Clin. **72**(3), 202–229 (2022).
4. A. Wahida, L. Buschhorn, S. Frohling, P. J. Jost, A. Schneeweiss, P. Lichter, and R. Kurzrock, "The coming decade in precision oncology: six riddles," Nat. Rev. Cancer. **23**(1), 43–54 (2023).
5. K. D. Miller, Q. T. Ostrom, C. Kruchko, N. Patil, T. Tihan, G. Cioffi, H. E. Fuchs, K. A. Waite, A. Jemal, R. L. Siegel, and J. S. Barnholtz-Sloan, "Brain and Other Central Nervous System Tumor Statistics, 2021," CA Cancer J. Clin. **71**(5), 381–406 (2021).
6. Z. Z. Zhang, L. B. E. Shields, D. A. Sun, Y. P. Zhang, M. A. Hunt, and C. B. Shields, "The art of intraoperative glioma identification," Front. Oncol. **5**, 175 (2015).
7. N. Verburg, P. J.W. Pouwels, R. Boellaard, F. Barkhof, O. S. Hoekstra, J. C. Reijneveld, W. P. Vandertop, P. Wesseling, and P. C. de Witt Hamer, "Accurate delineation of glioma infiltration by advanced PET/MR neuro-imaging (FRONTIER study): a diagnostic study protocol," Neurosurgery **79**(4), 535–540 (2016).
8. A. Selvapandian and K. Manivannan, "Fusion based glioma brain tumor detection and segmentation using ANFIS classification," Comput. Meth. Prog. Bio. **166**, 33–38 (2018).
9. Y. Wu, Z. Zhao, W. Wu, Y. Lin, and M. Wang, "Automatic glioma segmentation based on adaptive superpixel," BMC Med. Imaging **19**(1), 73 (2019).
10. M. A. Mishchenko, A. V. Lebedeva, T. A. Mishchenko, K. S. Yashin, L. S. Lepekhina, K. A. Astafyeva, I. P. Ivanova, M. V. Vedunova, I. A. Medyanik, and V. B. Kazantsev, "Field potentials recording in the brain tissue as a new criterion for determination of glial tumors boundaries," Sovrem. Technol. Med. **10**(3), 32–40 (2018).
11. E. Belykh, E. J. Miller, D. Hu, N. L. Martirosyan, E. C. Woolf, A. C. Scheck, V. A. Byvaltsev, P. Nakaji, L. Y. Nelson, E. J. Seibel, and M. C. Preul, "Scanning fiber endoscope improves detection of 5-aminolevulinic acide induced protoporphyrin IX fluorescence at the boundary of infiltrative glioma," World Neurosurg. **113**, e51–e69 (2018).
12. Z. Chen, X. Zhu, W. Zheng, Y. Xiang, Y. Huang, H. Fang, A. Deng, F. Yi, H. Chen, D. Han, and S. Lv, "Relationship between the sodium fluorescein yellow fluorescence boundary and the actual boundary of high-grade gliomas during surgical resection," Brit. J. Neurosurg. **2021**, 1 (2021).
13. F. Yan, J. Zhuang, Q. Yu, Z. Dou, X. Jiang, S. Tan, S. Han, X. Wu, Y. Zang, C. Li, J. Li, H. Chen, L. Hu, X. Li, and G. Chen, "Strategy of de novo design toward first-in-class imaging agents for simultaneously differentiating glioma boundary and grades," ACS Sens. **6**(9), 3330–3339 (2021).
14. D. Kong, W. Peng, R. Zong, G. Cui, and X. Yu, "Morphological and biochemical properties of human astrocytes, microglia, glioma, and glioblastoma cells using fourier transform infrared spectroscopy," Med. Sci. Monit. **26**, e925754 (2020).

15. G. Yang, K. Zhang, X. Qu, W. Xu, and S. Xu, "Ratiometric pH-responsive SERS strategy for glioma boundary determination," Talanta **250**, 123750 (2022).

16. Z. Yang, Y. Du, Q. Sun, Y. Peng, R. Wang, Y. Zhou, Y. Wang, C. Zhang, and X. Qi, "Albumin-based nanotheranostic probe with hypoxia alleviating potentiates synchronous multimodal imaging and phototherapy for glioma," ACS Nano **14**(5), 6191–6212 (2020).

17. O. Cherkasova, Y. Peng, M. Konnikova, Y. Kistenev, C. Shi, D. Vrazhnov, O. Shevelev, E. Zavjalov, S. Kuznetsov, and A. Shkurinov, "Diagnosis of glioma molecular markers by terahertz technologies," Photonics **8**(1), 22 (2021).

18. H. Fabelo, M. Halicek, S. Ortega, M. Shahedi, A. Szolna, J. F. Piñeiro, C. Sosa, A. J. O'Shanahan, S. Bisshopp, C. Espino, M. Márquez, M. Hernández, D. Carrera, J. Morera, G. M. Callico, R. Sarmiento, and B. Fei, "Deep learning-based framework for in vivo identification of glioblastoma tumor using hyperspectral images of human brain," Sensors **19**(4), 920 (2019).

19. H. Fabelo, S. Ortega, and A. Szolna, *et al.*, "In-vivo hyperspectral human brain image database for brain cancer detection," IEEE Access **7**, 39098–39116 (2019).

20. L. Guo, D. Zhang, L. Sun, S. Yao, L. Zhang, Z. Wang, Q. Wang, H. Ding, R. Zheng, Z. Hou, and Z. Wang, "Development in the application of laser-induced breakdown spectroscopy in recent years: A review," Front. Phys. **16**(2), 22500 (2021).

21. F. Xu, S. Ma, C. Zhao, and D. Dong, "Application of molecular emissions in laser-induced breakdown spectroscopy: a review," Front. Phys.-Lausanne **10**, 821528 (2022).

22. M. Al-Salihi, R. Yi, S. Wang, Q. Wu, F. Lin, J. Qu, and L. Liu, "Quantitative laser-induced breakdown spectroscopy for discriminating neoplastic tissues from non-neoplastic ones," Biomed. Opt. Express **29**(3), 4159–4173 (2021).

23. X. Lin, H. Sun, X. Gao, Y. Xu, Z. Wang, and Y. Wang, "Discrimination of lung tumor and boundary tissues based on laser-induced breakdown spectroscopy and machine learning," Spectrochim. Acta B **180**, 106200 (2021).

24. X. Chen, Y. Zhang, X. Li, Z. Yang, A. Liu, and X. Yu, "Diagnosis and staging of multiple myeloma using serum-based laser-induced breakdown spectroscopy combined with machine learning methods," Biomed. Opt. Express **12**(6), 3584–3596 (2021).

25. Z. Yue, C. Sun, F. Chen, Y. Zhang, W. Xu, S. Shabbir, L. Zou, W. Lu, W. Wang, Z. Xie, L. Zhou, Y. Lu, and J. Yu, "Machine learning-based LIBS spectrum analysis of human blood plasma allows ovarian cancer diagnosis," Biomed. Opt. Express **12**(5), 2559–2574 (2021).

26. Q. Wang, X. Chen, J. Zhang, G. Teng, X. Cui, B. S. Idrees, and K. Wei, "Primary study of identification of parathyroid gland based on laser-induced breakdown spectroscopy," Biomed. Opt. Express **12**(4), 1999–2014 (2021).

27. B. S. Idrees, Q. Wang, M. N. Khan, G. Teng, X. Cui, W. Xiangli, and K. Wei, "In-vitro study on the identification of gastrointestinal stromal tumor tissues using laser-induced breakdown spectroscopy with chemometric methods," Biomed. Opt. Express **13**(1), 26–38 (2022).

28. S. Zhang, Z. Hu, Z. Zhao, F. Chen, Y. Tang, Z. Sheng, D. Zhang, Z. Zhang, H. Jin, H. Pu, and L. Guo, "Quantitative analysis of mineral elements in hair and nails using calibration-free laser-induced breakdown spectroscopy," Optik **242**, 167067 (2021).

29. J.-H. Choi, S. Shin, Y. Moon, J. H. Han, E. Hwang, and S. Jeong, "High spatial resolution imaging of melanoma tissue by femtosecond laser-induced breakdown spectroscopy," Spectrochim. Acta B **179**, 106090 (2021).

30. K. Kiss, A. Sindelarova, L. Krbal, V. Stejskal, K. Mrazova, J. Vrabel, M. Kaska, P. Modlitbova, P. Porizka, and J. Kaiser, "Imaging margins of skin tumors using laser-induced breakdown spectroscopy and machine learning," J. Anal. At. Spectrom. **36**(5), 909–916 (2021).

31. G. Teng, Q. Wang, H. Zhang, W. Xiangli, H. Yang, X. Qi, X. Cui, B. S. Idrees, K. Wei, and M. N. Khan, "Discrimination of infiltrative glioma boundary based on laser-induced breakdown spectroscopy," Spectrochim. Acta B **165**, 105787 (2020).

32. G. Teng, Q. Wang, H. Yang, X. Qi, H. Zhang, X. Cui, B. S. Idrees, W. Xiangli, K. Wei, and M. N. Khan, "Pathological identification of brain tumors based on the characteristics of molecular fragments generated by laser ablation combined with a spiking neural network," Biomed. Opt. Express **11**(8), 4276–4289 (2020).

33. G. Teng, Q. Wang, X. Cui, G. Chen, K. Wei, X. Xu, B. S. Idrees, and M. N. Khan, "Predictive data clustering of laser-induced breakdown spectroscopy for brain tumor analysis," Biomed. Opt. Express **12**(7), 4438–4451 (2021).

34. X. Wang, M. Yao, M. Zeng, and J. Xu, "Detection model of copper based on polarization degree induced by low-energy density laser," Appl. Optics **60**(35), 10780–10784 (2021).

35. T. Wang and D. Zhao, "Stokes parameters of an electromagnetic light wave on scattering," Opt. Commun. **285**(6), 893–895 (2012).

36. A. Fan, T. Xu, X. Ma, J. Li, X. Wang, Y. Zhang, and C. Xu, "Four-dimensional compressed spectropolarimetric imaging," Signal Process. **195**, 108437 (2022).

37. A. Fan, T. Xu, J. Li, G. Teng, X. Wang, Y. Zhang, and C. Xu, "Compressive full-Stokes polarization and flexible hyperspectral imaging with efficient reconstruction," Opt. Laser. Eng. **160**, 107256 (2023).

38. E. K. Yeargers, "*Basic Biophysics for Biology*," (CRC Press, 1992).

39. F. Moynier, J. Creech, J. Dallas, and M. L. Borgne, "Serum and brain natural copper stable isotopes in a mouse model of Alzheimer's disease," Sci. Rep.-UK **9**(1), 11894 (2019).

40. P. Carmeliet and R. K. Jain, "Angiogenesis in cancer and other diseases," Nature **407**(6801), 249–257 (2000).

41. P. Carmeliet and R. K. Jain, "Molecular mechanisms and clinical applications of angiogenesis," Nature **473**(7347), 298–307 (2011).

42. P. L. Bedard, A. R. Hansen, M. J. Ratain, and L. L. Siu, "Tumour heterogeneity in the clinic," Nature **501**(7467), 355–364 (2013).

43. A. Shmatko, N. G. Laleh, M. Gerstung, and J. N. Kather, "Artificial intelligence in histopathology: enhancing cancer research and clinical oncology," Nat. Cancer **3**(9), 1026–1038 (2022).

44. J. Laak, G. Litjens, and F. Ciompi, "Deep learning in histopathology: the path to the clinic," Nat. Med. **27**(5), 775–784 (2021).

45. M. Ji, S. Lewis, S. Camelo-Piragua, S. H. Ramkissoon, M. Snuderl, S. Venneti, A. Fisher-Hubbard, M. Garrard, D. Fu, A. C. Wang, J. A. Heth, C. O. Maher, N. Sanai, T. D. Johnson, C. W. Freudiger, O. Sagher, X. S. Xie, and D. A. Orringer, "Detection of human brain tumor infiltration with quantitative stimulated Raman scattering microscopy," Sci. Transl. Med. **7**(309), 309ra163 (2015).

46. T. Fujimoto and A. Iwamae, "*Plasma Polarization Spectroscopy*," (Springer-Verlag, 2008).